

In preparation for ApJ.

Nonlinear Diffusive Shock Acceleration with Magnetic Field Amplification

Andrey Vladimirov and Donald C. Ellison

*Physics Department, North Carolina State University, Box 8202, Raleigh, NC 27695,
U.S.A.*

Andrei Bykov

*Department of Theoretical Astrophysics, Ioffe Physical-Technical Institute, St. Petersburg
RUSSIA*

`avladim@ncsu.edu, don_ellison@ncsu.edu, byk@astro.ioffe.rssi.ru`

ABSTRACT

We introduce a Monte Carlo model of nonlinear diffusive shock acceleration allowing for the generation of large-amplitude magnetic turbulence, i.e., $\Delta B \gg B_0$, where B_0 is the ambient magnetic field. The model is the first to include strong wave generation, efficient particle acceleration to relativistic energies in non-relativistic shocks, and thermal particle injection in an internally self-consistent manner. We find that the upstream magnetic field B_0 can be amplified by large factors and show that this amplification depends strongly on the ambient Alfvén Mach number. We also show that in the nonlinear model large increases in B do not necessarily translate into a large increase in the maximum particle momentum a particular shock can produce, a consequence of high momentum particles diffusing in the shock precursor where the large amplified field converges to the low ambient value. To deal with the field growth rate in the regime of strong fluctuations, we extend to strong turbulence a parameterization that is consistent with the resonant quasi-linear growth rate in the weak turbulence limit. We believe our parameterization spans the maximum and minimum range of the fluctuation growth and, within these limits, we show that the nonlinear shock structure, acceleration efficiency, and thermal particle injection rates depend strongly on the yet to be determined details of wave growth in strongly turbulent fields. The most direct application of our results will be to estimate magnetic fields amplified by strong cosmic-ray modified shocks in supernova remnants.

Subject headings: Supernova Remnants, cosmic rays, shock acceleration, X-ray and radio emission, MHD turbulence

1. INTRODUCTION

Recent observations and modeling of several young supernova remnants (SNRs) suggest the presence of magnetic fields at the forward shock (i.e., the outer blast wave) well in excess of what is expected from simple compression of the ambient circumstellar field, B_{CSM} . These large fields are inferred from (i) spectral curvature in radio emission (e.g., Reynolds & Ellison 1992; Berezhko et al. 1999), (ii) broad-band fits of synchrotron emission between radio and non-thermal X-rays (e.g., Berezhko et al. 2003; Völk, Berezhko & Ksenofontov 2005) (see also Cowsik & Sarkar 1980), and (iii) sharp X-ray edges (e.g., Vink & Laming 2003; Bamba et al. 2003; Völk, Berezhko & Ksenofontov 2005; Ellison & Cassam-Chenaï 2005). While these methods are all indirect, fields greater than $500 \mu\text{G}$ are inferred in Cas A and values of at least several $100 \mu\text{G}$ are estimated in Tycho, Kepler, SN1006, and G347.3-0.5. If $B_{\text{CSM}} \sim 3 - 10 \mu\text{G}$, amplification factors of 100 or more may be required to explain the fields immediately behind the forward shocks and this is likely the result of a nonlinear amplification process associated with the efficient acceleration of cosmic-ray ions via diffusive shock acceleration (DSA). The magnetic field strength is a critical parameter in DSA and also strongly influences the synchrotron emission from shock accelerated electrons. Since shocks are expected to accelerate particles in diverse astrophysical environments and synchrotron emission is often an important emission process (e.g., radio jets), quantifying the magnetic field amplification has become an important problem in particle astrophysics and has relevance beyond cosmic-ray production in SNRs.

If cosmic-ray (CR) production is as efficient as expected in theories of nonlinear DSA (e.g., Blandford & Eichler 1987; Jones & Ellison 1991; Malkov & Drury 2001), the CR pressure gradient in the shock precursor can do work on the incoming plasma and, in principle, place a large amount of energy in magnetic turbulence. In fact, if the DSA process is to work at all, magnetic turbulence must be self-generated on all resonant scale lengths to provide the scattering necessary to drive the particle distribution to isotropy. If the turbulence remains weak, i.e., if $\Delta B/B \ll 1$, the self-generation of turbulence by CR streaming in the shock precursor can be adequately described using quasi-linear theory (e.g., Skilling 1975; McKenzie & Völk 1982). For large amplitude turbulence, however, this analytic description becomes questionable and less rigorous approximations must be made.

In principle, a complete description of nonlinear DSA, including magnetic field amplification, is possible with particle-in-cell (PIC) simulations. In reality, however, these simula-

tions are still far too computationally demanding to produce realistic models of astrophysical sources such as supernova remnants. Approximate methods describing nonlinear DSA must be used. Here, we have developed a method which incorporates a phenomenological model of particle diffusion and turbulence growth (similar to Bell & Lucek 2001; Amato & Blasi 2006) in a fully nonlinear Monte Carlo model of DSA (e.g., Jones & Ellison 1991; Ellison, Baring & Jones 1996; Berezhko & Ellison 1999). While not a first-principles description of the plasma physics, the computational efficiency of our approach gives it a significant advantage over PIC simulations and semi-analytic techniques based on the diffusion approximation in that we can determine the shock structure, the injection of thermal particles, the acceleration of these particles to relativistic energies, and the magnetic turbulence, all self-consistently in a fully nonlinear steady-state model.

An important advantage of the Monte Carlo simulation is that, in effect, it solves a more basic set of equations governing the shock structure and DSA than do techniques based on diffusion–convection equations (e.g., Ellison & Eichler 1984). There is no assumption of isotropy for particle distributions and this allows an internally self-consistent treatment of thermal particle injection. Injection is still phenomenological and depends on the assumptions made for the particle pitch-angle scattering, but these assumptions are applied equally to all particles. Since there is only one set of scattering assumptions, the Monte Carlo technique eliminates a free “injection parameter” which is present in all models based on the diffusion approximation to set the injection efficiency. As we show, the strong feedback between injection, shock structure, and magnetic field amplification makes this property of the Monte Carlo technique particularly important.

Our preliminary results show that magnetic field amplification results in an increase in the maximum CR momentum, p_{\max} , a given shock system can produce compared to the case without amplification. For the case we consider, acceleration truncated by a finite-size shock, this increase is not, however, as large as the increase in B in the shocked region since fields on scales of the upstream diffusion length of the highest energy particles strongly influence p_{\max} . Furthermore, the fact that B ranges smoothly from the unshocked value far upstream, B_0 , to the amplified value, B_2 , downstream from the shock will have consequences for electrons since radiation losses will be greatest in the downstream region where particles spend a large fraction of their time.¹ Thus, the maximum momentum protons and electrons obtain may be determined by two very different field strengths.

¹We consistently use the subscript 0 for far upstream values, the subscript 2 for downstream values, and the subscript 1 for values immediately upstream from the subshock. Thus, the overall compression ratio is $r_{\text{tot}} = u_0/u_2$ and the subshock compression ratio is $r_{\text{sub}} = u_1/u_2$, where u is the bulk flow speed.

We also show that the amplification factor, B_2/B_0 , increases with Alfvén Mach number, that is, for a given shock speed and ambient density, a small B_0 will be amplified more than a larger B_0 . The ability to dramatically increase very low ambient fields may make it possible for reverse shocks in young SNRs to accelerate particles and produce relativistic electrons and radio synchrotron emission (see Ellison, Decourchelle & Ballet 2005, for a discussion of DSA at reverse shocks in SNRs). The injection and acceleration of electrons in amplified fields will be considered in subsequent work, here, we consider only proton acceleration.

In this paper, we demonstrate the feasibility of applying Monte Carlo techniques to DSA with field amplification, but have made a number of approximations regarding wave generation and have neglected wave damping. An important advantage of the Monte Carlo method is that it can be generalized to include more realistic descriptions of non-resonant wave growth, linear and nonlinear damping, and the calculation of the momentum and space dependent diffusion coefficient from the turbulent energy density, and work along these lines is in progress. While a more accurate description of the plasma physics will influence all aspects of the acceleration process, we expect that p_{\max} will be most strongly determined by the plasma physics details and thus will remain a critical problem for understanding the origin of galactic cosmic rays for some time.

2. MODEL

2.1. Assumptions for Magnetic Turbulence Generation

Consider a steady-state collisionless shock propagating along a uniform component \mathbf{B}_0 of a stochastic magnetic field \mathbf{B} . We only consider parallel shocks where \mathbf{B}_0 is along x and the shock face is perpendicular to \mathbf{B}_0 . As the unshocked plasma approaches the shock and experiences the pressure gradient in the cosmic-ray precursor, the energetic particles back-streaming from the shock cause fluctuations of the field, $\Delta\mathbf{B}$, to grow. In the linear regime, $\Delta\mathbf{B}$ is perpendicular to \mathbf{B}_0 and the local rate of growth of energy in waves is proportional to the pressure gradient. The plasma motion associated with these field fluctuations is initially Alfvénic: transverse and incompressible, and it will remain as such as long as $\Delta B \ll B_0$.

As the perturbations grow and reach $\Delta B \gtrsim B_0$, however, it is likely that waves with wave vectors \mathbf{k} not aligned with \mathbf{B}_0 will be generated, due to local CR pressure gradients along the total $\mathbf{B} = \mathbf{B}_0 + \Delta\mathbf{B}$. With $\Delta B \gtrsim B_0$, it becomes impossible to predict the average value of the transverse pressure gradients and the resulting magnetic field structure without knowing the relative phases of different wave harmonics. The problem is further complicated by the fact that this longitudinal, compressible turbulence may produce a strong second-order Fermi

particle acceleration effect which, in turn, can damp the longitudinal fluctuations (see, for example, Schlickeiser, Campeanu & Lerche 1993).

These complications place a precise description of plasma turbulence beyond current analytic capabilities and lead to our goal of obtaining a realistic approximation that includes the essential nonlinear effects from efficient DSA but still allows particle acceleration over a large dynamic range. In order to accomplish this, we consider two limiting cases. The first assumes there is no longitudinal turbulence, in which case the wave growth rate is determined by the Alfvén speed in the un-amplified field B_0 . This gives a lower bound to the growth rate. The upper limit assumes that the turbulence is isotropic, in which case the growth rate is determined by the Alfvén speed in the much larger amplified field B_{eff} (defined below). The real situation should lie between these two cases and while we consider these limits, we do not explicitly include second-order Fermi acceleration in our calculations.

To get an initial estimate of the shock structure, we use a Monte Carlo simulation of diffusive shock acceleration, assuming that the motion of particles can be described as pitch-angle scattering in the Bohm limit. The Monte Carlo simulation provides the distribution of fast particles at all positions relative to the viscous subshock and allows for a calculation of the particle pressure gradient, $\partial P_p(x, p)/\partial x$, which drives the amplification process in the shock precursor.² Then, we use $\partial P_p(x, p)/\partial x$ to calculate the total energy density in magnetic turbulence, $U_{\text{tot}}(x)$, as a function of position across the shock. This calculation uses the well-known equation for Alfvén wave growth (e.g., Skilling 1975; Völk, Drury & McKenzie 1984), i.e.,

$$u(x) \frac{\partial}{\partial x} U(x, k) = V_G \left[\frac{\partial P_p(x, p)}{\partial x} \frac{p}{k} \right]_{p=\bar{p}(k)}, \quad (1)$$

where $u(x)$ is the bulk flow speed of the plasma, p is the particle momentum, $U_{\text{tot}} = \int_0^\infty U(x, k) dk$, $\bar{p}(k)$ is the momentum of particles resonant with wavevector k , and much of the complicated plasma physics is contained in V_G , an unknown growth-rate coefficient with dimensions of speed. Once the wave energy density is determined (as described below), it is used to calculate an “effective” amplified magnetic field, $B_{\text{eff}}(x) \equiv \sqrt{4\pi U_{\text{tot}}(x)}$, and this field is then used to calculate the particle diffusion coefficient, $D(x, p)$, as a function of position and momentum.

For the growth of Alfvén waves in quasi-linear theory, $V_G = v_a$, where $v_a = B_0/\sqrt{4\pi\rho(x)}$ is the Alfvén speed calculated with the un-amplified field and $\rho(x)$ is the matter density

²It’s important to note that while we speak of “thermal” and “superthermal” particles, and may refer to superthermal particles as cosmic rays, the Monte Carlo simulation makes no distinction between thermal and superthermal particles. The same assumptions are applied to particles regardless of their energy.

at position x . As mentioned above, taking $V_G = v_a$ ignores the transverse gradients of pressure and only the component of the pressure gradient along the initial magnetic field B_0 is accounted for. This choice of V_G provides a lower limit on the amplification rate and was used in Amato & Blasi (2006). If, on the contrary, we define V_G using the amplified field, i.e., $V_G = B_{\text{eff}}(x)/\sqrt{4\pi\rho(x)}$, it reflects the situation where the growth rate is determined by the maximum gradient of $P_p(x, p)$ along the fluctuating field lines. This provides an upper limit on the wave growth rate and was used in Bell & Lucek (2001).

A similar argument applies to the resonance condition. In order to obtain a solution, we assume a resonance relation between k and p even though there is unlikely to be such a simple relation in strong turbulence. Again, we can define two limiting cases where the resonant wavelength for particles of momentum p lies between $\lambda_{\text{res}}(p) = r_g(B_0, p)$ and $\lambda_{\text{res}}(p) = r_g(B_{\text{eff}}, p)$, where $r_g = pc/(eB)$ is the gyroradius. The real situation should lie between the two extremes for V_G and λ_{res} . For this preliminary work, we set $\lambda_{\text{res}}(p) = r_g(B_0, p)$, but vary V_G between the two limits, i.e., we introduce a parameter, $0 \leq f_{\text{alf}} \leq 1$, such that

$$V_G = v_a \left\{ 1 + \left[\frac{B_{\text{eff}}(x)}{B_0} - 1 \right] f_{\text{alf}} \right\}, \quad (2)$$

and V_G varies linearly between v_a (for $f_{\text{alf}} = 0$) and $B_{\text{eff}}/\sqrt{4\pi\rho(x)}$ (for $f_{\text{alf}} = 1$).

Finally, we assume a Bohm model for diffusion. The mean free path of a particle with momentum p at position x is taken to be equal to the gyroradius of this particle in the amplified field, i.e., $\lambda(x, p) = r_g(x, p) = pc/[qB_{\text{eff}}(x)]$, and the diffusion coefficient is then $D(x, p) = \lambda v/3$, where v is the particle speed. Closure of the model is provided by using the newly calculated diffusion coefficient in the Monte Carlo simulation, calculating a new shock structure and pressure gradient profile $\partial P_p(x, p)/\partial x$, and iterating until mass, momentum, and energy fluxes are conserved throughout the shock.

2.2. Monte Carlo Simulation

The basic Monte Carlo simulation used here is described in detail in a number of papers including Jones & Ellison (1991) and Ellison, Jones & Reynolds (1990); Ellison, Jones & Baring (1999). The model calculates the shock structure and nonlinear particle spectrum self-consistently, including thermal particle injection. As mentioned above, injection can be treated self-consistently in this model because the Monte Carlo technique does not require the diffusion approximation and no distinction between thermal and superthermal particles is made. Until now, however, in parallel shocks we have assumed a spatially independent form for the diffusion coefficient, i.e., that the diffusion coefficient, $D(p)$, is proportional to

gyroradius: $D(p) = \lambda v/3$, where $\lambda = \eta r_{g,0}$ is the particle mean free path, $r_{g,0} = pc/(qB_0)$ is the gyroradius, and $\eta \geq 1$ is an arbitrary parameter determining the “strength” of scattering.³ In fact, we assume λ and then individual particles pitch-angle scatter with some maximum scattering angle which is set to give the assumed mean free path (see Ellison, Jones & Reynolds 1990; Ellison & Double 2004, for full details of the pitch-angle scattering process).

The Monte Carlo simulation obtains the shock structure $u(x)$ by iteration, ensuring that mass, momentum, and energy fluxes are conserved across the shock. When DSA is efficient, the shock is modified by the back pressure of accelerated particles and the flow speed, $u(x)$, becomes a “smooth” function of x , i.e., an upstream precursor with $P_p \sim \rho u^2$ forms. In addition to shock smoothing, the overall compression ratio of the shock, r_{tot} , will increase when the acceleration is efficient (e.g., Eichler 1984; Jones & Ellison 1991) and r_{tot} is obtained by iteration as well. Below, we show how our code has been generalized to include the modification of the diffusion coefficient by the buildup of magnetic turbulence.

2.3. Magnetic Field Amplification

To calculate the effect of the pressure gradient of particles on magnetic field fluctuations, we start with an equation similar to equation (B.8) in McKenzie & Völk (1982):

$$\frac{\partial}{\partial t} U_w + \frac{\partial}{\partial x} F_w = u \frac{\partial}{\partial x} P_w - v_{a,x} \frac{\partial P_{\text{cr}}}{\partial x} - \bar{L} . \quad (3)$$

Here $U_w = (\Delta B)^2/4\pi$ is the energy density of the waves (assuming that the kinetic energy density of shear wave motion equals the magnetic energy density), $F_w = (3u/2 - v_a)U_w$ is the wave energy flux (the 3/2 represents the sum of the Poynting flux and the flux associated with the transverse motion of plasma in Alfvén waves), $P_w = U_w/2$ is the magnetic pressure of waves acting on the plasma flow, and \bar{L} represents wave energy losses (or gains) due to processes other than compression and amplification by the considered instability, and $\partial P_{\text{cr}}/\partial x$ is the pressure gradient of cosmic rays exciting the Alfvén waves. This equation describes the growth of the energy in Alfvén waves through their instability in the presence of CR streaming, and it assumes that all the waves are moving upstream with respect to the plasma at speed v_a , so $v_{a,x} = -v_a$.

³Parallel shocks are those where the shock normal is parallel to the magnetic field direction and oblique shocks are ones where the field makes some angle to the normal. The MC simulation has been generalized for plane, oblique shocks, in which case B and D vary with x as the strength and angle the magnetic field makes with the shock normal vary (e.g., Ellison, Baring & Jones 1996; Ellison, Jones & Baring 1999; Ellison & Double 2004).

Now, following Bell & Lucek (2001), we separate the turbulence into downstream- and upstream-moving structures, and define the energy density of these structures per wavenumber interval as $U_+(x, k)$ and $U_-(x, k)$, respectively, so that the total energy density of turbulence is

$$U_{\text{tot}} = \int_0^\infty [U_-(x, k) + U_+(x, k)] dk . \quad (4)$$

We also define the partial pressure of particles with momentum p per unit momentum interval as $P_p(x, p)$ so that the total pressure in particles, including thermal ones, is

$$P_{p, \text{tot}} = \int_0^\infty P_p(x, p) dp . \quad (5)$$

To derive equations for $U_\pm(x, k)$, we apply a steady-state version of (3) to waves with wavenumber k in the interval Δk . For the energy density of these waves in the first order of Δk we substitute

$$U_w = [U_+(x, k) + U_-(x, k)] \Delta k . \quad (6)$$

For the energy flux, we write

$$F_w = \left[\left(\frac{3}{2}u(x) - V_G \right) U_-(x, k) + \left(\frac{3}{2}u(x) + V_G \right) U_+(x, k) \right] \Delta k , \quad (7)$$

and for the pressure of particles interacting with these waves,

$$P_{\text{cr}} = P_p(x, p) \Delta p . \quad (8)$$

Substituting these expressions into (3), ignoring the energy loss (gain) term \bar{L} , then dividing both sides by Δk and taking the limit $\Delta k \rightarrow 0$, we get

$$\begin{aligned} \frac{\partial}{\partial x} \left[\left(\frac{3}{2}u(x) - V_G \right) U_-(x, k) + \left(\frac{3}{2}u(x) + V_G \right) U_+(x, k) \right] = \\ u(x) \frac{\partial}{\partial x} \left(\frac{1}{2}U_-(x, k) + \frac{1}{2}U_+(x, k) \right) - v_{\text{wt}} \frac{\partial P_{\text{cr}}(x, p)}{\partial x} \left| \frac{dp}{dk} \right| , \end{aligned} \quad (9)$$

where we have replaced $v_{a,x}$ with a weighted wave speed

$$v_{\text{wt}}(x, k) \equiv V_G \frac{U_+(x, k) - U_-(x, k)}{U_+(x, k) + U_-(x, k)} , \quad (10)$$

in the driving term. Using v_{wt} is a logical extension of the definition of an “average” wave speed by Bell & Lucek (2001) applied to a narrow wavenumber range Δk . This, again, is justified as long as $\Delta k \ll B_0$, but becomes less clear for strong turbulence. In these equations, V_G is defined as in equation (2).

The coefficient $|dp/dk|$ that the driving term has acquired is necessary to relate the interval of wavenumbers Δk of amplified waves to the interval of momenta of particles interacting with these waves Δp . As mentioned above, the relationship between p and k (i.e., the resonant condition) is assumed to be $k = 1/r_{g,0}$, where $r_{g,0} = cp/(eB_0)$, and B_0 is the far upstream magnetic field. One may argue that the field that the particles ‘feel’ as uniform in the non-linear regime $\Delta B \gg B_0$ is the field carried by all long-wavelength (relative to the particle gyroradius) harmonics, rather than B_0 . While this may be true in general, our present model is insensitive to the choice of the resonance condition due to the simplified ‘Bohm’ form of the particle mean free path we assume.

Equation (9) expresses energy conservation and accounts for the amplification of turbulence by the streaming instability with the growth rate determined from kinetic theory. Furthermore, we assume, as did Bell & Lucek (2001), that interactions between the forward and backward moving waves drive them to isotropy on a time scale $\sim r_{g,0}/V_G$. In order to account for this interaction, we write equation (9) as the sum of the following two equations for $U_{\pm}(x, k)$:

$$[u(x) - V_G] \frac{\partial}{\partial x} U_- + U_- \frac{d}{dx} \left(\frac{3}{2} u(x) - V_G \right) = \frac{U_-}{U_+ + U_-} V_G \frac{\partial P_{\text{cr}}(x, p)}{\partial x} \left| \frac{dp}{dk} \right| - \frac{V_G}{r_{g,0}} (U_- - U_+) ; \quad (11)$$

$$[u(x) + V_G] \frac{\partial}{\partial x} U_+ + U_+ \frac{d}{dx} \left(\frac{3}{2} u(x) + V_G \right) = - \frac{U_+}{U_+ + U_-} V_G \frac{\partial P_{\text{cr}}(x, p)}{\partial x} \left| \frac{dp}{dk} \right| + \frac{V_G}{r_{g,0}} (U_- - U_+) , \quad (12)$$

which are solved iteratively in the MC simulation. We note that equations (11) and (12) are consistent with equation (9) without the relaxation terms on the right-hand sides of both equations, but these terms may become important in cases with small shock velocities.

Equations (11) and (12) are generalizations of those introduced by Bell & Lucek (2001). The generalization has two essential improvements. First, it accounts for the spatial dependence of flow speed $u(x)$ due to nonlinear effects of efficient DSA and, consequently, treats ‘compression’ of the amplified field adequately. To illustrate this effect, consider (11) and (12), neglecting the cosmic-ray pressure gradient term and v_a , i.e., taking $V_G \ll u$. Adding the two equations then results in

$$u(x) \frac{\partial}{\partial x} [U_- + U_+] + \frac{3}{2} [U_- + U_+] \frac{d}{dx} u(x) = 0 , \quad (13)$$

which can be easily integrated to give $[U_- + U_+] \propto u^{-3/2}$, or $B_{\text{eff}} \propto u^{-3/4}$. Consequently, in a shock with a total compression ratio $r_{\text{tot}} = 10$, for example, the stochastic magnetic field gets a boost in amplification by a factor of about 6 solely through the compression of the plasma. This compressional effect is especially important at the subshock and the change in magnetic turbulence energy density will influence the subshock compression ratio r_{sub} . This in turn will have a strong effect on the injection efficiency in the Monte Carlo model.

Second, we generalized the equations to describe the whole spectrum of turbulence $U_{\pm}(x, k)$ rather than a single waveband with $\Delta k = k$. We solve this system with a finite-difference method, integrating from far upstream ($x \rightarrow -\infty$) to x . The quantities $u(x)$ and $P_p(x, p)$ are obtained from the Monte Carlo simulation, as described in Section 2.2. For simplicity in this initial presentation of our model, and because the shocks we are mainly concerned with have high Alfvén Mach numbers ($v_a \ll u$), we have neglected V_G compared to u in the first and second terms in equations (11) and (12) in the numerical results we present here.⁴ We do, however, account for the wave or scattering center speed relative to the bulk flow speed in determining the energy change a particle receives as it scatters in the converging flow. In each interaction, we replace $u(x) \rightarrow u(x) + v_{\text{wt}}$, and since v_{wt} is generally negative in the upstream region (i.e., $U_- > U_+$), a finite v_{wt} dampens particle acceleration. Downstream from the shock we take $v_{\text{wt}} = 0$.

The initial condition for our equations is the far upstream magnetic turbulence spectrum $U(x \rightarrow \infty, k)$. We take

$$U_-(x \rightarrow -\infty, k) = U_+(x \rightarrow -\infty, k) = \begin{cases} A(k/k_c)^{-\alpha}, & k_c < k < k_m \\ 0, & k < k_c \text{ or } k > k_m, \end{cases} \quad (14)$$

where the limits k_m and k_c are chosen to encompass the range between the inverse gyroradii of thermal particles and the most energetic particles in the shock, respectively. For concreteness we take $\alpha = 1$, but none of our results depend in any substantial way on α , k_m , or k_c . Using our definition of the effective, amplified magnetic field,

$$B_{\text{eff}}^2(x) = 4\pi \int_0^{\infty} [U_-(x, k) + U_+(x, k)] dk, \quad (15)$$

the normalization constant A in equation (14) is determined by requiring that

$$4\pi \int_0^{\infty} [U_-(\infty, k) + U_+(\infty, k)] dk = B_0^2. \quad (16)$$

⁴In all of the examples in this paper, $V_G < 0.2u(x)$ in the shock precursor and $V_G < 0.5u_2$ in the post-shock region.

2.4. Particle Scattering

Once the amplified magnetic field is determined from equation (15), the scattering mean free path is set equal to the gyroradius of the particle in this field, i.e.,

$$\lambda(x, p) = \frac{cp}{eB_{\text{eff}}(x)} . \quad (17)$$

Equation (17) is essentially the Bohm limit and, as such, is a crude approximation. In a strong collisionless shock, modified by efficient DSA, a significant fraction of the energy is contained in high-momentum particles. These particles have long mean free paths and will resonantly produce turbulence where long-wavelength harmonics contain most of the wave energy. Consequently, to low-momentum particles, the strong long-wavelength turbulence appears approximately as a uniform field and equation (17) is justified. For the highest energy particles, however, equation (17) will overestimate the scattering strength since, for these particles, most of the harmonics of the magnetic field appear as short-scale fluctuations which are not very efficient at changing the particle's momentum. In this case, there is no reason to assume that the scattering is resonant, i.e., there is no simple resonance relation between k and p . This is a critical point since the form for $\lambda(x, p)$ at high p determines the maximum momentum that can be produced in a given shock system, and this is one of the important unsolved problems for DSA.

Clearly, more physically realistic models for both the diffusion coefficient and the resonance condition are required for future work. An approach for determining the mean free path of particles in strongly turbulent fields is described in Bykov & Toptygin (1992), where non-resonant scattering and diffusive transport of particles in large-scale fluctuations are taken into account. The model presented here, where the calculation of the power spectrum of turbulence $U_{\pm}(x, k)$ is coupled to the nonlinear shock structure, will be generalized to include more physically realistic wave-particle interactions in future work.

2.5. Momentum and Energy Conservation

The total energy density of the MHD turbulence is defined by equation (4), and it is assumed to be equally shared between the stochastic magnetic field and the incompressible transverse motion of the gas. The momentum flux of the turbulence is then the magnetic pressure, i.e.,

$$P_{w,\text{tot}}(x) = \frac{1}{2} \int_0^{\infty} [U_{-}(x, k) + U_{+}(x, k)] dk = \frac{1}{2} U_{\text{tot}}(x) . \quad (18)$$

The total energy flux in turbulence is

$$F_{w,\text{tot}}(x) = \int_0^\infty \left[\left(\frac{3}{2}u - V_G \right) U_-(x, k) + \left(\frac{3}{2}u + V_G \right) U_+(x, k) \right] dk , \quad (19)$$

or

$$F_{w,\text{tot}}(x) \approx \frac{3}{2}u(x)U_{\text{tot}}(x) , \quad (20)$$

in the limit $V_G(x) \ll u(x)$.

In order to determine the velocity profile, $u(x)$, consistent with the back-reaction of accelerated particles and turbulence on the flow, the Monte Carlo simulation solves the following equations expressing the conservation of mass and momentum fluxes, i.e.,

$$\rho(x)u(x) = \rho_0 u_0 , \quad (21)$$

$$\rho(x)u(x)^2 + P_{p,\text{tot}}(x) + P_{w,\text{tot}}(x) = \rho_0 u_0^2 + P_{p0} + P_{w0} \equiv P_0 , \quad (22)$$

where $P_{p,\text{tot}}(x)$ is the pressure produced by all particles, thermal and superthermal and P_0 is the far upstream momentum flux. The particle pressure is related to $P_p(x, p)$ by equation (5), and is calculated in the simulation directly from the trajectories of individual particles. The energy flux conservation relation is

$$\frac{\rho(x)u(x)^3}{2} + F_{p,\text{tot}}(x) + F_{w,\text{tot}}(x) + q_{\text{esc}} = \frac{\rho_0 u_0^3}{2} + F_{p0} + F_{w0} \equiv F_0 , \quad (23)$$

where $F_{p,\text{tot}}(x)$ is the energy flux in all particles, q_{esc} is the energy flux lost by particles leaving the system at the upstream free escape boundary (FEB), and F_0 is the far upstream energy flux. In parallel shocks, $u(x)$ can be determined from equations (21) and (22) alone. The relation between r_{tot} and q_{esc} (i.e., eq. 10 in Ellison, Moebius & Paschmann 1990) allows equation (23) to be used to check the consistency of the simulation results, as we show with the examples below.

3. RESULTS

In all of the following examples we set the shock speed $u_0 = 5000 \text{ km s}^{-1}$, the unshocked proton number density $n_{p0} = 1 \text{ cm}^{-3}$, and the unshocked proton temperature $T_0 = 10^6 \text{ K}$. For simplicity, the electron temperature is set to zero and the electron contribution to the jump conditions is ignored. With these parameters, the sonic Mach number $M_s \simeq 43$ and the Alfvén Mach number $M_{\text{alf}} \simeq 2300(1\mu\text{G}/B_0)$.

3.1. With and Without Magnetic Field Amplification

In order to obtain a solution which conserves momentum and energy fluxes, both the shock structure, i.e., $u(x)$, and the overall compression ratio, r_{tot} , must be obtained self-consistently. Figure 1 shows results for four shocks where $u(x)$ and r_{tot} have been determined with the iterative method described above. In all examples in this section, $f_{\text{alf}} = 0$. First, we compare the results shown with heavy-weight solid curves to those shown with heavy-weight dotted curves. The heavy solid curves were determined with B -field amplification while the dotted curves were determined with a constant $B_{\text{eff}}(x) = B_0$. All other input parameters were the same for these two models, i.e., $B_0 = 30 \mu\text{G}$, $f_{\text{alf}} = 0$ (i.e., minimum wave amplification), and an upstream free escape boundary at $d_{\text{FEB}} = -10^4 r_g(u_0)$, where $r_g(u_0) \equiv m_p u_0 c / (e B_0)$. The most striking aspect of this comparison is the increase in $B_{\text{eff}}(x)$ when field amplification is included (bottom panels). The magnetic field goes from $B_{\text{eff}}(x \rightarrow -\infty) = 30 \mu\text{G}$, to $B_{\text{eff}} > 1000 \mu\text{G}$ for $x > 0$, and this factor of > 30 increase in B will influence the shock structure and the particle distributions in important ways. Note that there is about a factor of ~ 2 jump in B at the subshock. As shown in Section 2.3, the jump in B at the subshock from compression (ignoring the contribution from the particle pressure gradient) is $B_2/B_1 \sim (u_1/u_2)^{3/4} = r_{\text{sub}}^{3/4}$, where u_1 is the flow speed immediately upstream from the subshock and the subshock compression ratio is defined as $r_{\text{sub}} = u_1/u_2$. For the heavy-weight solid curve in Figure 1, $r_{\text{sub}} \simeq 2.7$ and $B_2/B_1 \sim 2$, as observed.

The solution without B -field amplification (dotted curves) has a considerably larger r_{tot} than the one with amplification, i.e., for no B -field amplification, $r_{\text{tot}} \simeq 22$, and with B -field amplification (heavy solid curves), $r_{\text{tot}} \simeq 11$.⁵ This difference in overall compression results because the wave pressure $P_{w,\text{tot}}$ in equation (22) is much larger in the field amplified case making the plasma less compressible.

Two effects cause r_{tot} to increase above the test-particle limit of 4 for strong shocks. The first is the production of relativistic particles which produce less pressure for a given energy density than non-relativistic particles making the plasma more compressible. The second, and most important, is the escape of energetic particles at the FEB. As indicated in the energy flux panels of Figure 1, the energy flux drops abruptly at $x \sim d_{\text{FEB}}$ as energetic particles diffuse past the FEB and escape the system. The energy lost from the escaping particles is analogous to radiation losses in radiative shocks and results in an increase in compression ratio. For high Mach number parallel shocks, $1/r_{\text{tot}} \sim [5 - (9 + 16q_{\text{esc}}/F_0)^{1/2}]/8$

⁵See Berezhko & Ellison (1999) for a discussion of how very large r_{tot} 's can result in high Mach number shocks if only adiabatic heating is included in the precursor. The uncertainty on the compression ratios for the examples in this paper is typically $\pm 10\%$.

(Ellison, Moebius & Paschmann 1990), so for the dotted curves $r_{\text{tot}} = 22$ and $q_{\text{esc}} \simeq 0.8F_0$, and for the heavy solid curves $r_{\text{tot}} = 11$ and $q_{\text{esc}} \simeq 0.5F_0$, consistent with the energy fluxes shown in Figure 1.

The momentum flux is also conserved, but the escaping momentum flux is a much smaller fraction of the upstream value than for energy (Ellison 1985). Any departures from the far upstream momentum flux seen in Figure 1 are less than the statistical uncertainties in the simulation. As mentioned above, we only include adiabatic heating in the upstream precursor. If wave damping and heating were included, it is expected that r_{tot} would be reduced from what we see with wave amplification alone.

For a given shock, an increase in r_{tot} must be accompanied by a decrease in the sub-shock compression ratio, r_{sub} (see, for example, Berezhko & Ellison 1999, for a discussion of this effect). A large r_{tot} means that high energy particles with long diffusion lengths get accelerated very efficiently and, therefore, the fraction of particles injected must decrease accordingly to conserve energy. The shock structure adjusts so weakened injection (i.e., a small r_{sub}) just balances the more efficient acceleration produced by a large r_{tot} . Since r_{sub} largely determines the plasma heating, the more efficiently a shock accelerates particles causing r_{tot} to increase, the less efficiently the plasma is heated. For the cases shown in Figure 1, $r_{\text{sub}} \simeq 3.8$ for the amplified field case (heavy solid curves) and $r_{\text{sub}} \simeq 2.4$ for the case with no B -field amplification (heavy dotted curves).

In Figure 2 we show the phase space distributions, $f(p)$, for the shocks shown in Figure 1. For the two cases with the same parameters except field amplification, we note that the amplified field case (heavy solid curve) obtains a higher p_{max} and has a higher shocked temperature (indicated by the shift of the “thermal” peak and caused by the larger r_{sub}) than the case with no field amplification (heavy dotted curves). It is significant that the increase in p_{max} is modest even though B increases by more than a factor of 30 with field amplification. We emphasize that p_{max} as such is not a parameter in this model; p_{max} is determined self-consistently once the size of the shock system, i.e., d_{FEB} , and the other environmental parameters are set.

In order to show the effect of changing d_{FEB} , we include in Figs. 1 and 2 field amplification shocks with the same parameters except that d_{FEB} is changed to $-1000 r_g(u_0)$ (dashed curves) and $-10^5 r_g(u_0)$ (light-weight solid curves). From Figure 2, it’s clear that p_{max} scales approximately as d_{FEB} and that the concave nature of $f(p)$ is more pronounced for larger p_{max} . The field amplification also increases with p_{max} , but the increase between the $d_{\text{FEB}} = -1000 r_g(u_0)$ and $d_{\text{FEB}} = -10^5 r_g(u_0)$ cases is less than a factor of two (bottom panels of Figure 1).

In Figure 3 we show the energy density in magnetic turbulence, $U_+(x, k) + U_-(x, k)$, the diffusion coefficient, $D(x, p)$, and particle distributions all at various positions in the shock. All of these plots are for the example shown with dashed curves in Figs. 1 and 2. The bottom panel shows how $f(x, p)$ varies in the precursor where particles must diffuse upstream against the incoming plasma. The upstream diffusion length, $[D(x, p)/u(x)]_{\text{ave}}$, is some weighted average which is determined directly in the Monte Carlo simulation. The diffusion coefficients, shown in the middle panel, are determined from B_{eff} (equation 15), where the $U(x, k)$'s (top panel) are determined by solving equations (11) and (12) self-consistently with the shock structure using the particle pressure gradients determined from $f(x, p)$. The decrease in D by ~ 40 between far upstream and downstream from the shock corresponds to the increase in B_{eff} shown with the dashed curve in the bottom panel of Figure 1. The top panel clearly shows the spread in k where resonant interactions produce wave growth at the different x -positions, including the portion from thermal particles at high k .

The efficiency of the shock acceleration process is shown in Figure 4. The curves on the left give the number density of particles with momentum greater than p [$N(> p)$], and the curves on the right give the energy density in particles with momentum greater than p [$E(> p)$]. Both sets of curves are determined solely from the downstream particle distributions (calculated in the shock reference frame) shown in Figs. 1 and 2 with heavy solid and dotted curves. Thus they ignore escaping particles and the energy in magnetic turbulence. Nevertheless, these curves indicate that the shocks are extremely efficient accelerators with $> 50\%$ of the energy density in $f(p)$ placed in relativistic particles (i.e., $p \geq m_p c$). The actual energy efficiencies are considerably higher since the escaping particles carry away a larger fraction of the total energy than is placed in magnetic turbulence. With q_{esc} included, well over 50% of the total shock energy is placed in relativistic particles. Despite this high energy efficiency, the fraction of total particles that become relativistic is small, i.e., $N(> p = m_p c) \sim 10^{-5}$ in both cases.

The effect of magnetic field amplification on the number of particles injected is evident in the left-hand curves. The larger r_{sub} (solid curve) results in more downstream particles being injected into the Fermi mechanism with amplification than without. While it is hard to see from Figure 4, when the escaping energy flux is included, the shock with B -field amplification puts a considerably smaller fraction of energy in relativistic particles than the shock without amplification. Again, injection depends in a nonlinear fashion on the shock parameters and the subshock strength will adjust to ensure that just the right amount of injection occurs so that momentum and energy are conserved.

3.2. Alfvén Mach Number Dependence

In Figure 5 we show three examples where B_0 has been varied from 0.3 to 3 to 30 μG ; all other input parameters are kept constant including the physical distance to the FEB and $f_{\text{alf}} = 0$. For these examples, $|d_{\text{FEB}}| = 1.7 \times 10^{10} \text{ m} = 5.6 \times 10^{-7} \text{ pc}$. In units of $r_g(u_0) = m_p u_0 / (e B_0)$, the units used for the x -coordinates in Figs. 1 and 5, this corresponds to $|d_{\text{FEB}}| = 1000, 100$, and $10 r_g(u_0)$, for $B_0 = 0.3, 3$, and $30 \mu\text{G}$, respectively. The top four panels showing $u(x)/u_0$ and energy flux have the same format as the corresponding panels in Figure 1. As in Figure 1, q_{esc} is significant and $r_{\text{tot}} > 7$ in all cases. The magnetic field panels differ from Figure 1 in that here we plot $B(x)/B_0$ and it's clear that the amplification of B is greatest for the lowest B_0 , i.e., $B(x)/B_0$ increases with increasing M_{alf} . For the examples shown here, $B_2/B_0 \simeq 400$ for $B_0 = 0.3 \mu\text{G}$, $B_2/B_0 \simeq 150$ for $B_0 = 3 \mu\text{G}$, and $B_2/B_0 \simeq 30$ for $B_0 = 30 \mu\text{G}$. In the bottom panels, we show the pressure in magnetic turbulence, $P_{\text{w,tot}}$, divided by the total far upstream momentum flux, P_0 . For these examples, $P_{\text{w,tot}}/P_0 \lesssim 0.1$ and the magnetic pressure stays well below equipartition with the gas pressure.

In Figure 6a we show the distribution functions corresponding to the shocks shown in Figure 5. As expected, the shock with the highest $B_0 = 30 \mu\text{G}$ yields the highest p_{max} . This p_{max} , however, is only about a factor of 5 greater than that for $B_0 = 0.3 \mu\text{G}$ obtained in a shock system of the same physical size. In Figure 6b we show the distribution functions for three cases where we have kept the upstream FEB boundary at the same number of gyroradii, i.e., $d_{\text{FEB}} = -100 r_g(u_0)$. In this case, the situation with p_{max} is reversed with the $B_0 = 0.3 \mu\text{G}$ shock obtaining the highest p_{max} . This is a combination of the fact that the physical size of the shock system is largest and that the field amplification is greatest for $B_0 = 0.3 \mu\text{G}$. The shock structure results are similar to those shown in Figure 5.

Table 1: Effect of varying f_{alf} . The errors on r_{tot} and r_{sub} are typically $\pm 10\%$.

f_{alf}	r_{tot}	r_{sub}	B_2/B_0	$kT_{\text{sub}}/(m_p u_0^2)$
0	9	3.7	30	0.12
0.1	8	3.9	40	0.1
0.5	6	4.3	50	3×10^{-2}
1	5	4.4	40	5×10^{-3}

3.3. Wave Amplification factor, f_{alf}

All of the examples shown so far have used the minimum amplification factor $f_{\text{alf}} = 0$. We now investigate the effects of varying f_{alf} between 0 and 1 so that V_G varies between $v_a(x)$ and $B_{\text{eff}}(x)/\sqrt{4\pi\rho(x)}$. The other shock parameters are the same as used for the dashed curves in Figure 1, i.e., $u_0 = 5000 \text{ km s}^{-1}$, $B_0 = 30 \mu\text{G}$, and $d_{\text{FEB}} = -1000 r_g(u_0)$.

Figure 7 shows $u(x)/u_0$ and $B_{\text{eff}}(x)/B_0$ for $f_{\text{alf}} = 0, 0.1, 0.5$, and 1 as indicated. The top panels show that increasing the growth rate (increasing f_{alf} and therefore V_G) produces a large change in the shock structure and causes the overall shock compression ratio, r_{tot} , to decrease. The decrease in r_{tot} signifies a decrease in the acceleration efficiency and a decrease in the fraction of energy that escapes at the FEB, and the subshock compression adjusts to ensure conservation of momentum and energy. The values for r_{tot} and r_{sub} are given in Table 1.

In contrast to the strong modification of $u(x)$, there is little difference in B_{eff}/B_0 (bottom panels of Figure 7) and little change in p_{max} (Figure 8), between these examples.

The fact that increasing the wave growth rate decreases the acceleration efficiency shows the nonlinear nature of the wave generation process and comes about for two reasons. The most important is that the magnetic pressure term in equation (22), $P_{w,\text{tot}}$, becomes significant compared to $\rho(x)u^2(x)$ when $f_{\text{alf}} \rightarrow 1$. The wave pressure causes the shock to be less compressive and forces r_{tot} down. Any change in r_{tot} changes the acceleration efficiency and therefore changes $\partial P_{\text{cr}}(x, p)/\partial x$, the wave growth, and the shock structure. The second reason is that as the turbulence grows, v_{wt} grows and the effective scattering center speed $u(x) + v_{\text{wt}}$ drops, causing the acceleration efficiency to drop. For the examples shown in Figure 7, the change produced by v_{wt} is modest compared to the effect from $P_{w,\text{tot}}$. Taken together, at least for the parameters used here, the increase in $P_{w,\text{tot}}$ and v_{wt} outweigh any increase in efficiency the amplified field produces.

The modified shock structure results in a significant change in the post-shock temperature. In Figure 8 we show the distribution functions for the four examples of Figure 7 and a change in temperature is seen with the shift of the thermal peaks. Using $3kT_s = m_p\Delta u^2$, where k is Boltzmann's constant and $\Delta u = u_1 - u_2$, we define the post-shock temperature, T_s , with

$$\frac{kT_s}{m_p u_0^2} = \frac{1}{3}(r_{\text{sub}} - 1)^2 , \quad (24)$$

and these values are listed in Table 1. For this set of examples, there is a spread in T_s of a factor ~ 25 between the cases with $f_{\text{alf}} = 0$ and 1.

As we have emphasized, the injection efficiency, i.e., the fraction of particles that enter the

Fermi process, must adjust to conserve momentum and energy. In Figure 9 we show $N(>p)$, the fraction of particles with momenta greater than p for the four cases in Figs. 7 and 8. The first point to notice is that the injection point separating thermal and superthermal particles is not well defined. This is a consequence of the fact that the MC doesn't distinguish between “thermal” and “nonthermal” particles. Once the shock has become smooth, the injection process is smooth and the superthermal population smoothly emerges from the quasi-thermal population.⁶ Nevertheless, the approximate momentum where the superthermal population develops, p_{inj} , can be estimated and we mark this position for the two extreme cases of $f_{\text{alf}} = 0$ and 1 with solid dots. This illustrates that p_{inj} shifts, *relative to the post-shock distribution*, when f_{alf} is varied and implies that, if injection is parameterized, the parameterization must somehow be connected to modifications in the shock structure.

4. SUMMARY AND COMPARISON WITH ALTERNATIVE MODELS

We have generalized a steady-state Monte Carlo model of efficient diffusive shock acceleration to include magnetic wave growth, allowing the wave amplitude to become large compared to the ambient field, i.e., $\Delta B/B_0 \gg 1$. The model uses a phenomenological treatment of wave generation by applying the linear growth rate formalism in the non-linear regime, but couples the nonlinear shock structure, the injection rate of thermal particles, the magnetic field amplification, and the determination of the maximum momentum particles obtain from a physical constraint, i.e., the size of the shock system, in an internally self-consistent manner.

Important limitations of our model are the simplified treatment of wave growth and the neglect of wave damping. We also assume a Bohm-like expression for the scattering mean free path [i.e., $\lambda(x, p) = pc/(eB_{\text{eff}})$] rather than calculating $D(x, p)$ from more fundamental relations which account for particle motions in strongly anisotropic turbulence. More physically realistic models for turbulence generation and damping and particle scattering are certainly necessary and may well modify the results we present here. However, it is not straightforward to include these processes in nonlinear models and, to our knowledge, none have yet been presented with as extensive nonlinear coupling as we calculate. We believe the approximations we make are an important intermediate step and that the results we present are indicative of what more complete models will show. The fact that the MC technique can

⁶We note that the smooth emergence of a superthermal tail has been seen in spacecraft observations of the quasi-parallel Earth bow shock (i.e., Ellison, Moebius & Paschmann 1990) and at interplanetary traveling shocks (i.e., Baring et al. 1997).

handle anisotropic particle distributions will be essential for including more precise plasma physics in future generalizations.

4.1. Particle-In-Cell Simulations

The difference between our Monte Carlo simulation and a particle-in-cell (PIC) plasma simulation is that the pitch-angle diffusion is treated phenomenologically in the MC with an assumed scattering mean free path, rather than calculating particle trajectories in the self-generated magnetic field obtained directly from Maxwell's equations. This approximation is essential in order to make the MC technique fast enough to model acceleration over a wide dynamic range. We emphasize that while PIC simulations, in principle, can solve the shock acceleration problem completely, their computational requirements are extreme and they are not yet capable of modeling acceleration over a dynamic range large enough to model cosmic sources such as SNRs. The most important constraint on PIC simulations is that they must be done fully in three dimensions. As shown by Jokipii, Kota & Giacalone (1993) and Jones, Jokipii & Baring (1998), PIC simulations with one or more ignorable dimensions artificially confine particles to field lines and eliminate cross-field diffusion, an essential ingredient in diffusive shock acceleration, particularly in oblique shocks. The 3-D requirement means that all three box dimensions must be increased to accommodate high-energy particles with long diffusion length scales so that computing requirements become insurmountable for a large enough dynamic range. To model SNR shocks, they must be able to accelerate particles from thermal to highly relativistic energies and, if electrons are to be modeled, they must simultaneously include electron and proton scales.⁷ While PIC simulations will be able to investigate important problems, particularly those concerning injection, they will not be able to model the shock acceleration of electrons and protons to the energies necessary to produce broad-band radiation with parameters similar to those of SNRs in the foreseeable future. Until then, progress can be made with approximate methods.

⁷We note that the computational requirements for the relativistic shocks expected in γ -ray-bursts may actually be less stringent than those for the non-relativistic shocks in SNRs. In shocks with large Lorentz factors, particles start off relativistic (in the shock frame) and can gain a great deal of energy in just a few shock interactions. It is also possible that electron–positron plasmas dominate the γ -ray-burst fireball so that important results can be obtained without simultaneously covering electron–proton scales. In the non-relativistic shocks present in SNRs, however, both electrons and protons must be accelerated over a wide dynamic range from eV to TeV energies by crossing the shock many times.

4.2. Semi-Analytic Models with B-field Amplification

Besides the limited results from PIC simulations, the only models of magnetic field generation with $\Delta B \gg B_0$ in nonlinear DSA that we are aware of are the semi-analytic results of Bell & Lucek (2001), Bell (2004, 2005), Ptuskin & Zirakashvili (2003), and Amato & Blasi (2006).

As we have mentioned, our work uses the same basic wave generation formalism as Bell & Lucek (2001), with an extensive generalization to include injection, nonlinear shock structure and particle distributions, and p_{\max} . More recently, Bell (2004, 2005) has attempted to improve the plasma physics by calculating amplified fields from a so-called “directly driven” mode of wave instability.⁸ In this scheme, upstream energetic particles standing in the shock frame produce a macroscopic current, and magnetic field, in the upstream plasma frame. This extended the Bell & Lucek (2001) analysis to wave modes other than resonant Alfvénic ones and emphasized that turbulence is likely the result of strongly driven, non-resonant modes at shorter wavelengths rather than Alfvén waves. While this is a promising idea for a non-resonant mechanism for wave amplification in strong shocks, careful consideration of the plasma return current must be made (e.g., F.C. Jones, private communication).

Another important attempt at describing turbulence with $\Delta B/B \gg 1$ was made by Ptuskin & Zirakashvili (2003, 2005). These authors assumed a Kolmogorov-type nonlinear wave growth and damping of self-generated turbulence by ion-neutral collisions. Most importantly, they obtained estimates for p_{\max} in a time-dependent analytic calculation. Nonlinear particle acceleration was assumed, but the analytic method required a number of approximations including the spatial distribution of energetic particles in the shock precursor and the spectral form of the energetic particles. Nevertheless, this work showed that nonlinear particle acceleration, combined with B -field amplification, may strongly influence p_{\max} , one of the most important parameters in diffusive shock acceleration.

In our estimation, the most highly developed model of nonlinear DSA with magnetic field amplification is that of Amato & Blasi (2006); work based on a series of papers by Blasi and co-workers (i.e., Blasi 2002, 2004; Blasi et al. 2005; Amato & Blasi 2005).⁹ We now

⁸Lucek & Bell (2000) and Bell (2004, 2005) also performed PIC simulations coupled to a 3-D MHD model of the background plasma. These results clearly showed that seed B -fields can be amplified by orders of magnitude but they were limited in dynamic range and did not self-consistently model the particle acceleration process.

⁹We note that Amato & Blasi (2005, 2006) use a different technique from the previous Blasi et al. work that allows an exact solution for an arbitrary choice of both the spatial and momentum dependent diffusion coefficient.

give a detailed comparison between that model and ours. The underlying assumptions for DSA are the same in both models, i.e., particles are driven to isotropy by interactions with magnetic turbulence in the background plasma. Particles gain energy when they diffuse in the converging flow and neither model includes second-order Fermi acceleration. Both models are also for plane-parallel, steady-state shocks.

The most important difference revolves around the method of solution. We use a Monte Carlo technique while Blasi et al. solve a transport or diffusion-convection equation. In the Blasi et al. work, macroscopic quantities (pressure, energy flux, etc.) are derived as moments of the particle distribution function $f(x, p)$, which is assumed to be isotropic in the shock reference frame. In contrast, the Monte Carlo simulation traces the stochastic motion of individual particles as they pitch-angle scatter off the background turbulence and calculates $f(x, p)$ and its moments directly from the particle trajectories without making any assumptions about the isotropy of $f(x, p)$. In effect, the MC simulation solves the more fundamental Boltzmann equation (e.g., Ellison & Eichler 1984). Of course, the semi-analytic technique is much faster computationally than the Monte Carlo technique and this will be important for building models in many applications.

Injection can be treated self-consistently in the MC simulation because, once the pitch-angle scattering assumptions are made, they are applied equally to all particles and the number and energy of injected particles is fully determined. No distinction is made between thermal and superthermal particles and the viscous subshock is assumed to be transparent so there is a nonzero probability for any downstream particle with $v > u_2$ to be injected. The diffusion approximation, on the other hand, with its assumption of isotropy forces additional assumptions if injection is to be modeled. Blasi et al. treat the subshock as having a finite thickness comparable to a thermal particle's gyroradius and the injection rate is parameterized such that only those particles get injected if their gyroradius is large enough to span the subshock. While this adds an additional parameter independent of the diffusion properties, it has been shown that parameters can easily be determined so that the Monte Carlo and semi-analytic models give similar results (see Ellison, Blasi & Gabici 2005).

Another important difference is that Amato & Blasi (2006) have included a phenomenological description of turbulent B -field heating, similar in implementation to that used in Berezhko & Ellison (1999), in addition to adiabatic heating. We only include adiabatic heating. The amplified turbulence may be dissipated through collisional and/or collisionless mechanisms and these include: (i) linear and nonlinear Landau damping (e.g., Akhieser et al. 1975; Achterberg & Blandford 1986; Kulsrud 1978; Vainshtein, Bykov & Toptygin 1993; Zirakashvili 2000), (ii) particle trapping (e.g., Medvedev 1999), and (iii) ion-neutral wave damping (e.g., Drury, Duffy & Kirk 1996; Bykov & Toptygin 2005). It's important to note

that even though the damping rates tend to be smaller than the wave growth rate (e.g., Bykov & Toptygin 2005), so that the generation of magnetic energy density can be approximately balanced solely by the convection of that turbulence through the shock (as was assumed here), the heating of the precursor plasma by dissipation modifies the subshock Mach number (e.g., Ellison, Berezhko & Baring 2000) and this in turn modifies injection. The overall acceleration efficiency and, of particular importance for X-ray observations, the temperature of the shocked plasma (e.g., Decourchelle, Ellison & Ballet 2000; Hughes, Rakowski & Decourchelle 2000; Ellison, Decourchelle & Ballet 2004) will depend on wave dissipation. We plan to include physically realistic models of wave damping in the MC simulation in future work.

The two most important elements in these nonlinear models is the turbulence generation and the diffusion coefficient that is derived from it. The assumptions for wave generation by the streaming instability are essential identical in the Blasi et al. model and ours.¹⁰ The most important difference in the models lies in the calculation of the mean free path and diffusion coefficient. Here, we assume Bohm-like diffusion with B_{eff} (equation 17), while Amato & Blasi (2006) use a mean free path due to resonant scattering that, in our notation, would be

$$\lambda_{\text{res}}(x, p) = \frac{cp}{eB_0} \frac{1}{2\pi^2 k_{\text{res}}} \frac{B_0^2}{[U_-(x, k_{\text{res}}) + U_+(x, k_{\text{res}})]}, \quad (25)$$

where

$$k_{\text{res}} = \frac{1}{r_{g,0}} = \frac{eB_0}{cp} \quad (26)$$

is the resonant wavenumber. Both of these assumptions are only formally valid for weak turbulence so an important step in advancing the state-of-the-art of nonlinear shock acceleration must center on improving the connection from wave generation to diffusion.

That important aspects of DSA are sensitive to the assumptions made for diffusion can be seen by comparing the self-generated $D(x, p)$ from these two models. Our use of equation (17) forces Bohm-like diffusion with $D(x, p)(x, p) \propto vp$ and we show this dependence in Figure 3. Nevertheless, we have argued in Section 2.4 that equation (17) overestimates the scattering strength for the highest momentum particles because most of the harmonics appear as short-scale fluctuations to these particles. This would suggest that the actual p dependence of $D(x, p)$ increases with p . In Amato & Blasi (2006), on the other hand, the momentum dependence of $D(x, p)$ is shown to weaken at high p to the point where the scattering becomes

¹⁰There is a minor difference in that Amato & Blasi (2006) assume that all waves generated by the streaming instability move upstream whereas we consider the interaction between waves moving upstream and downstream.

strong enough that $D(x, p)$ becomes independent of p in high sonic Mach number shocks. Since the behavior of $D(x, p)$ at high p determines p_{\max} , as well as influencing all other aspects of the shock acceleration process, it's clear that much work remains to be done on this difficult problem.

4.3. Other Models of Non-linear Shock Acceleration Without B-field Amplification

There are a number of nonlinear models of DSA besides those discussed above. However, none of these models include B -field amplification.

In a series of papers, Berezhko and co-workers have applied a model of nonlinear DSA to broad-band observations of several young SNRs (e.g., Berezhko et al. 1996, 2002). They used a time-dependent solution of the cosmic-ray transport equation coupled to the gas dynamic equations in spherical symmetry and calculated the superthermal proton distribution, from the forward shock, at all positions in the remnant. From this they can determine the overall contribution a single SNR makes to the galactic cosmic-ray proton flux. Furthermore, since they included the acceleration of superthermal electrons, they calculated the photon emission from synchrotron and IC processes, as well as from proton-proton interactions and pion-decay. This allowed them to fit the broad-band photon observations and constrain the model parameters. Of particular importance is their emphasis that magnetic fields much greater than typical ISM values are required to match broad-band photon observations. Equally important is their prediction, based on their fits, that TeV photon emission from several SNRs is most likely the result of pion-decay from protons rather than IC from electrons (e.g., Berezhko et al. 2003).

This model has been extremely successful and has added to our understanding of SNRs, but it does make important approximations and simplifications. The model assumes Bohm diffusion, parameterizes the number of injected particles, and does not include wave generation.¹¹

¹¹That B -field amplification is *not* included in the Berezhko et al. model can easily be missed, particularly since the titles of some of these papers, e.g., “Confirmation of strong magnetic field amplification and nuclear cosmic ray acceleration in SN 1006” (Berezhko et al. 2003), might suggest that the model does contain B -field amplification. The model of Berezhko et al. is a parallel shock model where the magnetic field is *not* explicitly included in the convection-diffusion equations. There is no B -field amplification and the large downstream fields that Berezhko et al. infer from matching the observations are obtained by an ad hoc compression of the upstream field (see, for example, the discussion before equation (8) in Völk et al. 2002). To obtain $300\,\mu\text{G}$ downstream, for example, they must start with an unshocked field of $\sim 50\,\mu\text{G}$ which is then compressed by

Other nonlinear shock models include those of Kang and Jones and co-workers (e.g., Kang, Jones & Gieseler 2002; Kang & Jones 2006), Malkov and co-workers (e.g., Malkov 1997; Malkov & Drury 2001; Malkov, Diamond & Jones 2002; Malkov & Diamond 2006), and the cosmic ray–hydrodynamical (CR-hydro) model of Ellison and co-workers (e.g., Ellison, Decourchelle & Ballet 2004). These models all involve different computational techniques, and all have their particular strengths and weaknesses. They have also been shown to produce similar nonlinear effects to those of Berezhko et al., and have been shown to be in quantitative agreement with our Monte Carlo model (before the addition of B -amplification). Since none of these models yet include B -field amplification we do not discuss them further.

5. CONCLUSIONS

We have introduced a model of diffusive shock acceleration which couples thermal particle injection, nonlinear shock structure, magnetic field amplification, and the self-consistent determination of the maximum particle momentum. This is a first step toward a more complete solution and, in this preliminary work, we make a number of approximations dealing mainly with the plasma physics of wave growth. Keeping in mind that our results are subject to the validity of our approximations, we reach a number of interesting conclusions.

First, our calculations find that efficient shock acceleration can amplify ambient magnetic fields by large factors and are generally consistent with the large fields believed to exist at blast waves in young SNRs, although we have not attempted a detailed fit to SNR observations in this paper. While the numerical values we obtain depend on the particular parameters for our examples, and we will investigate in detail how the amplification depends on sonic Mach number age and size of the shock system, etc., in future work, amplification factors of several 100 are clearly possible.

More specifically, we find that the amplification, in terms of the downstream to far upstream field ratio B_2/B_0 is a strong function of Alfvén Mach number, with weak ambient fields being amplified more than strong ones. For the range of examples shown in Figure 5, $B_2/B_0 \sim 30$ for $M_{\text{alf}} \sim 80$ and $B_2/B_0 \sim 400$ for $M_{\text{alf}} \sim 8000$.

This sharp M_{alf} dependence should not depend strongly on our approximations and may have important consequences. In young SNRs, the expansion of the ejecta material will drastically reduce any original circumstellar magnetic field. In fact, for any conceivable progenitor, the magnetic field inside of the reverse shock will drop to values too low to support

the shock with a ratio typically $r_{\text{tot}} \sim 6$ for their models.

the acceleration of electrons to radio emitting energies only a few years after the explosion (e.g., Ellison, Decourchelle & Ballet 2005). Evidence for radio emission at reverse shocks in SNRs has been reported (see, Gotthelf et al. 2001, for example) and the strong amplification of low fields we see here, may make it possible for reverse shocks in young SNRs to accelerate electrons to relativistic energies and produce radio synchrotron emission. If similar effects occur in relativistic shocks, these large amplification factors will be critical for the internal shocks presumed to exist in γ -ray bursts (GRBs). Even if large B -field amplification is confined to non-relativistic shocks, which tend to be more efficient accelerators than relativistic ones, amplification will be important for understanding GRB afterglows since the expanding fireball will slow as it moves through the interstellar medium and will always go through trans-relativistic and non-relativistic phases.

As expected, amplifying the magnetic field leads to a greater maximum particle momentum, p_{\max} , a given shock can produce. Quantifying p_{\max} is one of the outstanding problems in shock physics because of the difficulty in obtaining parameters for typical SNRs that allow the production of cosmic rays to energies at and above the CR knee near 10^{15} eV. Assuming that acceleration is truncated by the size of the shock system, we determine p_{\max} from a physical constraint: the relevant parameter is the distance to the free escape boundary in diffusion lengths. This means that the limit on acceleration feeds back on the shock structure and also mimics, in terms of the spectral shape, what happens in actual shocks where $f(x, p)$ must turn over smoothly at the highest energies (as in Figure 6). The spectral shape will be particularly important if the model is applied to the knee of the cosmic-ray spectrum or to nonthermal X-ray emission in SNRs.

Our results show that p_{\max} does increase when field amplification is included, but the increase is considerably less than the amplification factor at the shock B_2/B_0 (compare the heavy dotted and heavy solid curves in Figure 2). The main reason for this is that high momentum particles have long diffusion lengths and the precursor magnetic field well upstream from the subshock strongly influences p_{\max} . We calculate the spatial structure of the amplified magnetic field (Figs. 1 and 5) and, as expected, field amplification is greatest near the subshock and B_{eff} merges into the ambient field far upstream. The diffusion length that determines p_{\max} (i.e., $[D(x, p_{\max})/u(x)]_{\text{ave}}$) is some weighted average over the varying $u(x)$ and $B_{\text{eff}}(x)$ and is considerably greater than that estimated from B_2 alone. If the shock size, in our case d_{FEB} , limits acceleration, p_{\max} will be considerably less than crude estimates using a spatially independent B_2 .

On the other hand, particles spend a large fraction of their time downstream from the shock where the field is high and collision times are short. If shock age limits acceleration rather than size, we expect the increase in p_{\max} from the amplified field to be closer to the

amplification factor, B_2/B_0 . Thus, the spatial structure of the precursor field and $u(x)$, in addition to the overall amplification of B , will determine the relative time spent upstream versus downstream and will determine p_{\max} for a given shock system. This will be even more critical for electrons than for ions since electrons experience synchrotron and inverse-Compton losses which will mainly occur downstream. Again, the qualitative nature of the above conclusions should not depend on the particular parameters and approximations we make here. We leave more detailed quantitative work for future study.

Finally, it is well known that DSA is inherently efficient. Field amplification reduces the fraction of shock ram kinetic energy that is placed in relativistic particles but, at least for the limited examples we show here, the overall acceleration process remains extremely efficient. Even with large increases in B_0 , well over 50% of the shock energy can go into relativistic particles (Figure 4). As in all self-consistent calculations, the injection efficiency must adjust to conserve momentum and energy. In comparing shocks with and without field amplification, we find that field amplification lowers r_{tot} and, therefore, individual energetic particles are, on average, accelerated less efficiently. In order to conserve momentum and energy, this means that more thermal particles must be injected when amplification occurs. The shock accomplishes this by establishing a strong subshock which not only injects a larger fraction of particles, but also more strongly heats the downstream plasma. This establishes a nonlinear connection between the field amplification, the production of cosmic rays, and the X-ray emission from the shocked heated plasma.

The authors are grateful to F.C. Jones and P. Blasi for useful discussions. DCE acknowledges support from a NASA ATP grant (ATP02-0042-0006) and a NASA LTSA grant (NNH04Zss001N-LTSA), and AB was supported, in part, by RBRF 06-02-16844.

REFERENCES

Achterberg, A. & Blandford, R. D. 1986, MNRAS, 218, 551

Akhieser, A.I., Akhieser, I.A., Polovin, R.V., Sitenko, A.G. & Stepanov, K.N. 1975, “Plasma Electrodynamics”, Pergamon Press, Oxford

Amato, E. & Blasi, P. 2005, MNRAS, 364, L76

Amato, E. & Blasi, P. 2006, MNRAS, in press

Bamba, A., Yamazaki, R., Ueno, M. & Koyama, K. 2003, ApJ, 589, 827

Baring, M. G., Ogilvie, K. W., Ellison, D. C. & Forsyth, R. J. 1997, *ApJ*, 476, 889

Bell, A. R. 2004, *MNRAS*, 353, 550

Bell, A. R. 2005, *MNRAS*, 358, 181

Bell, A. R. & Lucek, S.G. 2001, *MNRAS*, 321, 433

Berezhko, E.G. & Ellison, D.C. 1999, *ApJ*, 526, 385

Berezhko, E. G., Elshin, V. K., & Ksenofontov, L. T. 1996, *JETP*, 82, 1

Berezhko, E. G., Ksenofontov, L. T. & Petukhov, S. I. 1999, Proc. 26th Int. Cosmic-Ray Conf.(Salt Lake City), 4, 431

Berezhko, E. G., Ksenofontov, L. T. & Völk, H. J. 2002, *A&A*, 395, 943

Berezhko, E. G., Ksenofontov, L. T. & Völk, H. J. 2003, *A&A*, 412, L11

Blandford, R. & Eichler, D. 1987, *Physics Reports*, 154, 1

Blasi, P. 2002, *Astroparticle Physics*, 16, 429

Blasi, P. 2004, *Astroparticle Physics*, 21, 45

Blasi, P., Gabici, S. & Vannoni, G. 2005, *MNRAS*, 361, 907

Bykov, A. M. & Toptygin, I. N. 1992, *Sov.Phys. JETP*, 74, 462

Bykov, A. M. & Toptygin, I. N. 2005, *Astronomy Letters*,

Cowsik, R. & Sarkar, S. 1980, *MNRAS*, 191, 855

Decourchelle, A. Ellison, D.C. & Ballet, J. 2000, *ApJ*, 543, L57

Drury, L. O'C., Duffy, P. & Kirk, J. G. 1996, *A&A*, 309, 1002

Eichler, D. 1984, *ApJ*, 277, 429

Ellison, D.C. 1985, *J. Geophys. Res.*, 90, 29

Ellison, D. C., Baring, M. G. & Jones, F. C. 1996, *ApJ*, 473, 1029

Ellison, D.C. Berezhko, E.G. & Baring, M.G. 2000, *ApJ*, 540, 292

Ellison, D. C., Blasi, P. & Gabici, S. 2005, proc. 29th ICRC (Puna, India), astro-ph/0507107

Ellison, D. C. & Cassam-Chenaï, G. 2005, *ApJ*, 632, 920

Ellison, D.C., Decourchelle, A. & Ballet, J. 2004, *A&A*, 413, 189

Ellison, D.C., Decourchelle, A. & Ballet, J. 2005, *A&A*, 429, 569

Ellison, D. C. & Double, G. P. 2002, *Astroparticle Physics*, 18, 213

Ellison, D. C. & Double, G. P. 2004, *Astroparticle Physics*, 2, 323

Ellison, D. C. & Eichler, D. 1984, *ApJ*, 286, 691

Ellison, D. C., Jones, F. C. & Baring, M. G. 1999, *ApJ*, 512, 403

Ellison, D. C., Jones, F. C. & Reynolds, S. P. 1990, *ApJ*, 360, 702

Ellison, D. C., Moebius, E. & Paschmann, G. 1990, *ApJ*, 352, 376

Gotthelf, E. V., Koralesky, B., Rudnick, L., Jones, T. W., Hwang, U. & Petre, R. 2001, *ApJ*, 552, L39

Hughes, J. P., Rakowski, C. E. & Decourchelle, A. 2000, *ApJ*, 543, L61

Jokipii, J. R., Kota, J. & Giacalone, J. 1993, *Geophys. Res. Lett.*, 20, 1759

Jones, F. C. & Ellison, D. C. 1991, *Space Science Reviews*, 58, 259

Jones, F. C., Jokipii, J. R. & Baring, M. G. 1998, *ApJ*, 509, 238

Kang, H. & Jones, T. W. 2006, *Astroparticle Physics*, 25, 246

Kang, H., Jones, T. W. & Gieseler, U. D. J. 2002, *ApJ*, 579, 337

Kulsrud, R. M. 1978, *Astronomical Papers Dedicated to Bengt Stromgren*, eds. Reiz, A. and Andersen, T. p. 317

Lucek, S. G. & Bell, A. R. 2000, *MNRAS*, 314, 65

Malkov, M. A. 1997, *ApJ*, 485, 638

Malkov, M. A. & Diamond, P. H. 2006, *ApJ*, 642, 244

Malkov, M. A., Diamond, P. H. & Jones, T. W. 2002, *ApJ*, 571, 856

Malkov, M. A. & Drury, L.O'C. 2001, *Reports of Progress in Physics*, 64, 429

McKenzie, J. F. & Völk, H. J. 1982, *A&A*, 116, 191

Medvedev, M. V. 1999, Physics of Plasmas, 6, 2191

Ptuskin, V. S. & Zirakashvili, V. N. 2003, A&A, 403, 1

Ptuskin, V. S. & Zirakashvili, V. N. 2005, A&A, 429, 755

Reynolds, S. P. & Ellison, D. C. 1992, ApJ, 399, L75

Schlickeiser, R., Campeanu, A. & Lerche, L. 1993, A&A, 276, 614

Skilling, J. 1975, MNRAS, 172, 557

Völk, H. J., Berezhko, E. G., Ksenofontov, L. T. & Rowell, G. P. 2002, A&A, 409, 563

Vainshtein, S. I., Bykov, A. M. & Toptygin, I. 1993, “Turbulence, current sheets, and shocks in cosmic plasma”, Gordon and Breach Science Publishers, Langhorne, Pa., U.S.A.

Vink, J. & Laming, J. M. 2003, ApJ, 584, 758

Völk, H. J., Drury, L. O. & McKenzie, J. F. 1984, A&A, 130, 19

Völk, H. J., Berezhko, E. G. & Ksenofontov, L. T. 2005, A&A, 433, 229

Zirakashvili, V. N. 2000, JETP, 90, 810

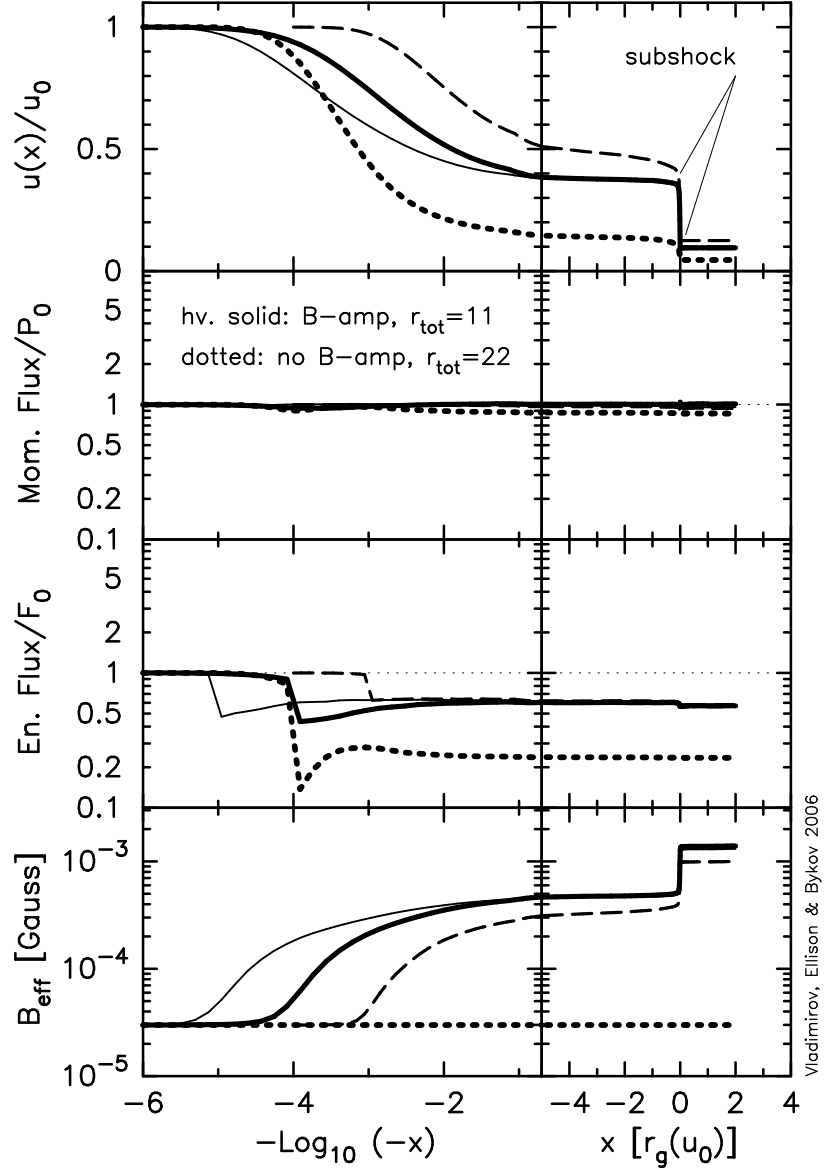


Fig. 1.— Shock structure including momentum and energy fluxes (in units of far upstream values) and the effective magnetic field vs. x . Note that the horizontal scale has units of $r_g(u_0) = m_p u_0 / (e B_0)$ and is divided at $x = -5r_g(u_0)$ between a linear and log scale. In all panels, the heavy dotted curves show results without amplification and all other curves are with amplification. The curves showing the energy flux drop sharply at the upstream FEB, which is at $-10^4 r_g(u_0)$ for the heavy solid and dotted curves, at $-1000 r_g(u_0)$ for the dashed curves, and at $-10^5 r_g(u_0)$ for the light solid curves, as particles freely leave the system. When this escaping flux is included, energy and momentum are conserved to within $\pm 10\%$.

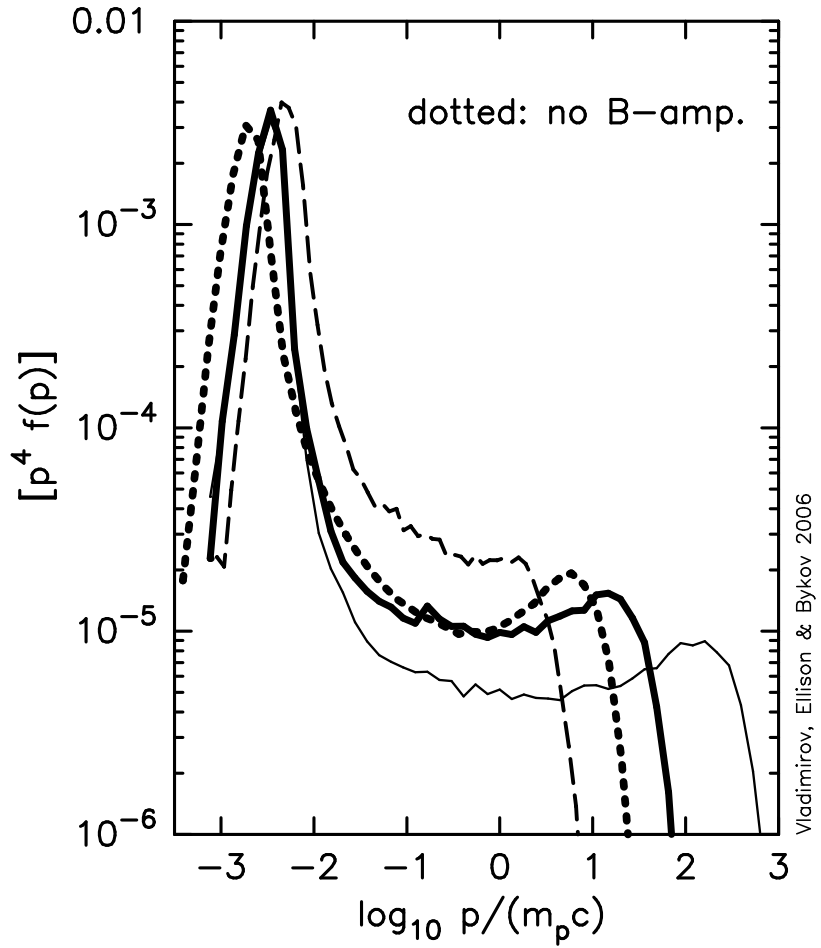


Fig. 2.— Phase space distributions for the shocks shown in Figure 1. These spectra are multiplied by $[p/(m_p c)]^4$ and are calculated downstream from the shock in the shock rest frame. As in Figure 1, the heavy solid and dotted curves have $d_{\text{FEB}} = -10^4 r_g(u_0)$, the dashed curve has $d_{\text{FEB}} = -1000 r_g(u_0)$, the light solid curve has $d_{\text{FEB}} = -10^5 r_g(u_0)$.

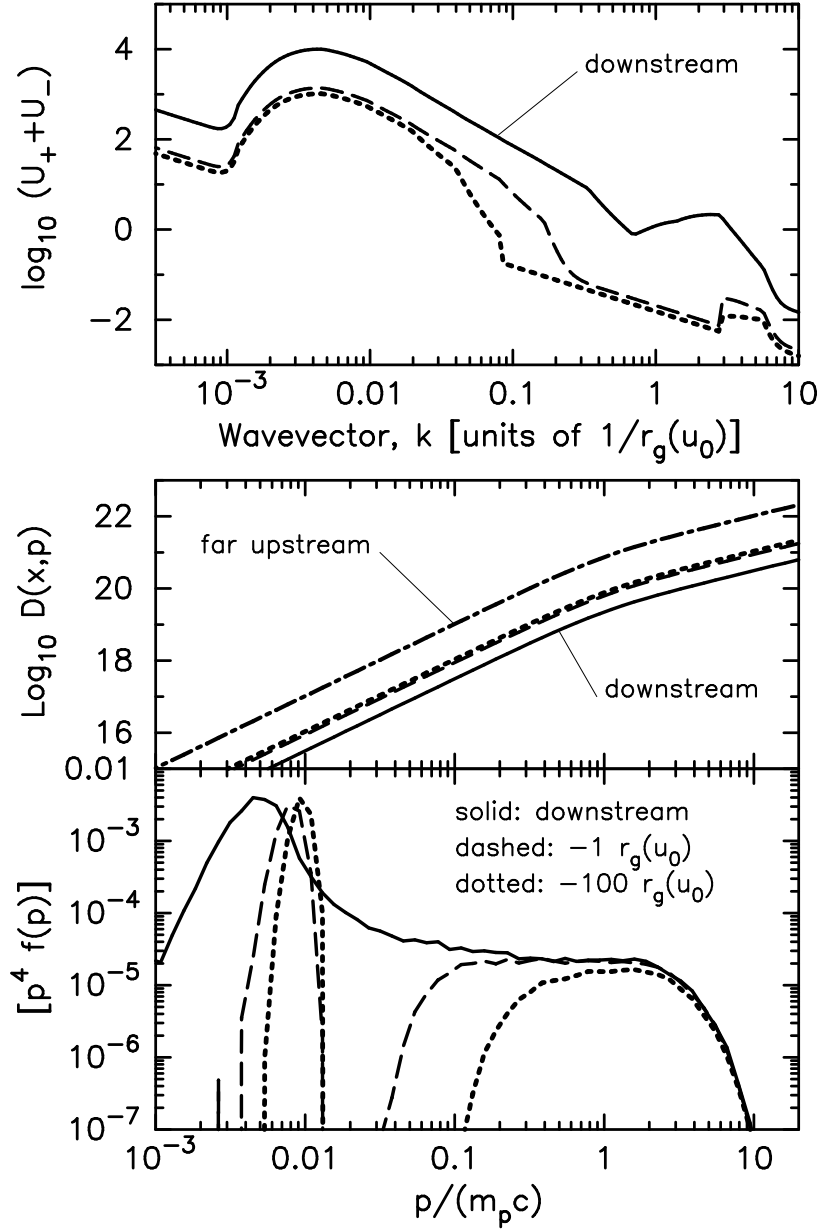


Fig. 3.— The top panel shows $U_+(x, k) + U_-(x, k)$ vs. k at three positions relative to the subshock. Here and in the other two panels, the solid curve is calculated downstream from the shock, the dashed curve is calculated at $x = -r_g(u_0)$ upstream from the subshock, and the dotted curve is calculated at $x = -100r_g(u_0)$ upstream from the subshock. The middle panel shows the diffusion coefficient with an additional dash-dotted curve showing the far upstream value. The bottom panel shows the distribution functions, multiplied by $[p/(m_pc)]^4$, at the various positions.

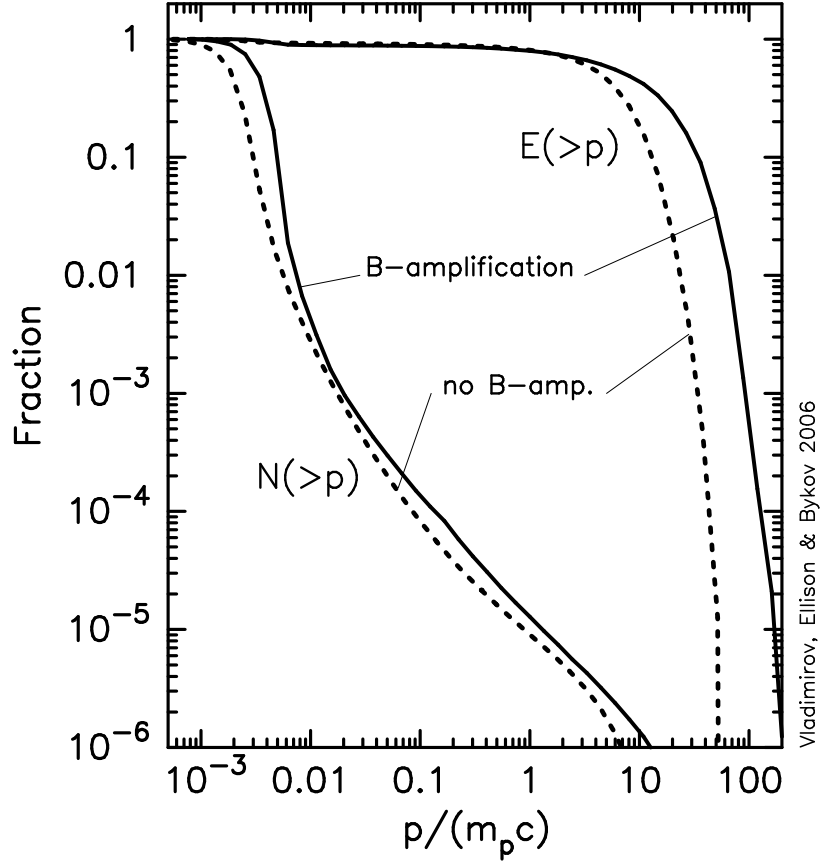


Fig. 4.— The left-hand curves show the fraction of particles with momentum greater than p , while the right-hand curves show the fraction of energy density in particles with momentum greater than p , for the shocks shown in Figs. 1 and 2 with heavy solid and dotted curves. These curves are calculated from the distributions shown in Figure 2 and do not include the particles that escaped at d_{FEB} . While the number fraction of escaping particles is small, the energy fraction is significant, as indicated in Figure 1. The solid curves show results with field amplification and the dotted curves show results without field amplification, both with $d_{\text{FEB}} = -10^4 r_g(u_0)$.

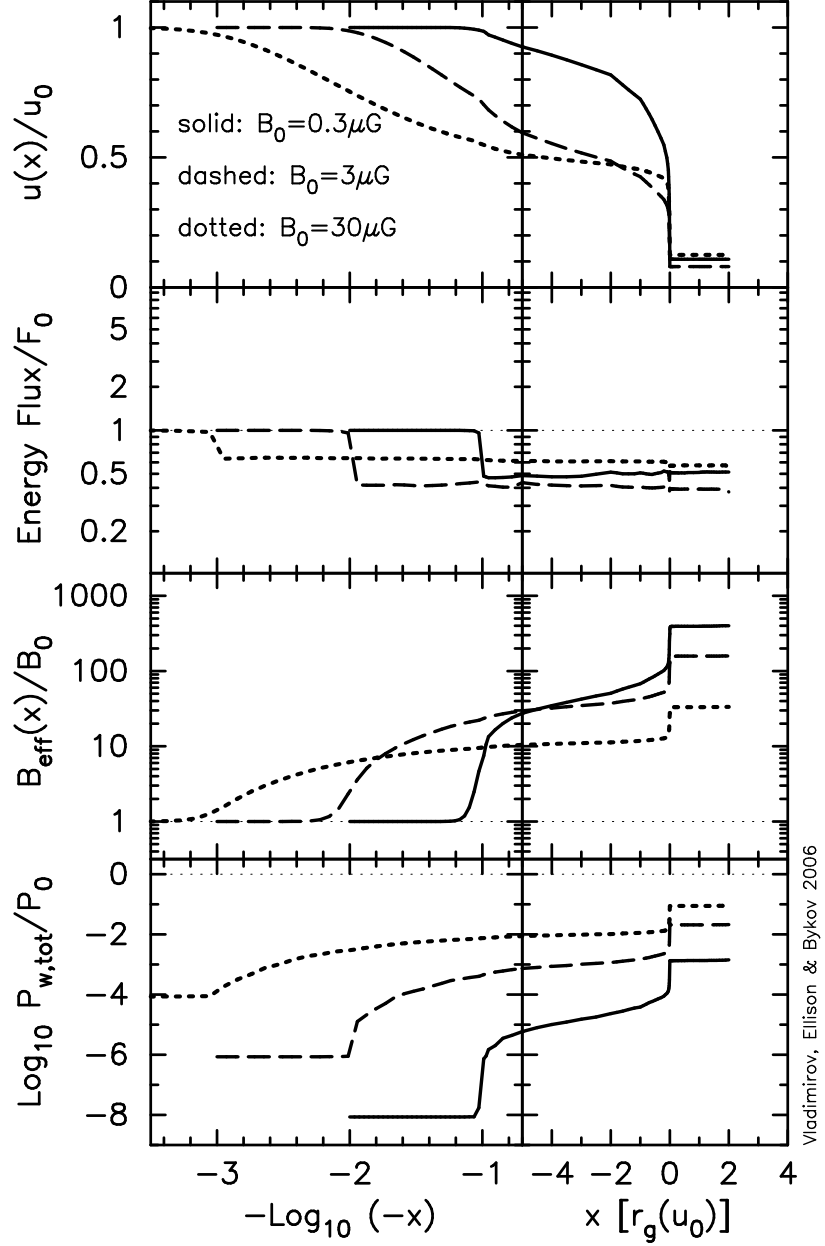


Fig. 5.— Comparison of shocks with different far upstream fields B_0 . In all panels, the solid curves are for $B_0 = 0.3 \mu\text{G}$, the dashed curves are for $B_0 = 3 \mu\text{G}$, and the dotted curves are for $B_0 = 30 \mu\text{G}$. The FEB is placed at the same physical distance in all cases with $d_{\text{FEB}} = 1.7 \times 10^{10} \text{ m}$. The horizontal axis is in units of $r_g(u_0) \equiv m_p c / (e B_0)$, and is split at $x = -5r_g(u_0)$ between a linear and logarithmic scale. Note that B_{eff} increases most strongly for $B_0 = 0.3 \mu\text{G}$, but that the pressure in magnetic turbulence never gets above $\sim 10\%$ of the total pressure. The overall compression ratios are: $r_{\text{tot}} \simeq 9$ for $B_0 = 0.3 \mu\text{G}$, $r_{\text{tot}} \simeq 12$ for $B_0 = 3 \mu\text{G}$, $r_{\text{tot}} \simeq 8$ for $B_0 = 30 \mu\text{G}$, values consistent, within statistical errors, with q_{esc} , as indicated in the energy flux panels.

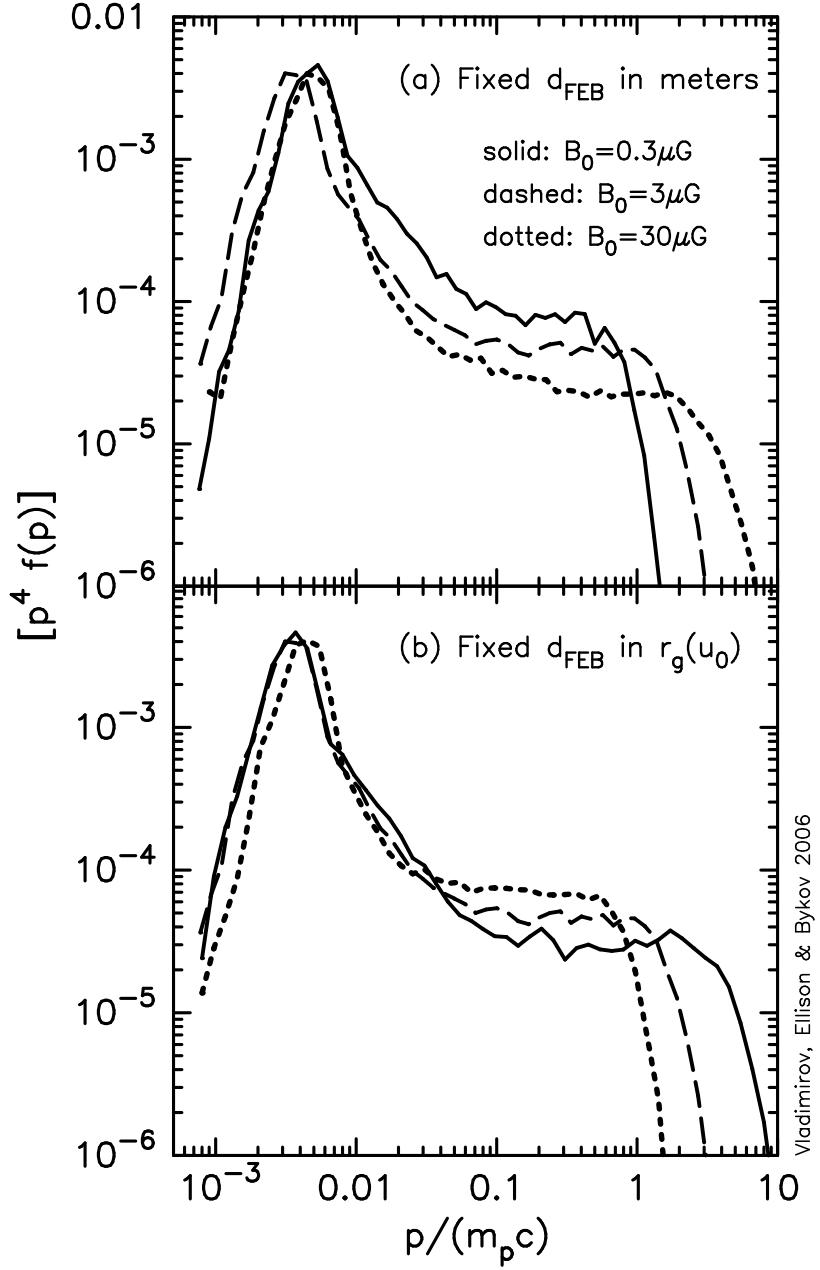


Fig. 6.— The top panel shows the distribution functions obtained in the shock frame in the downstream regions of the shocks shown in Figure 5. These shocks have the FEB at the same physical distance from the subshock and the shock with $B_0 = 30 \mu\text{G}$ produces the greatest p_{max} . In the bottom panel we show a similar set of curves only here, the FEB was set at a fixed $d_{\text{FEB}} = -100r_g(u_0)$ upstream. In this case, the shock with $B_0 = 0.3 \mu\text{G}$ produces the greatest p_{max} , a result of the larger shock size and greater amplification factor the high M_{alf} shock receives.

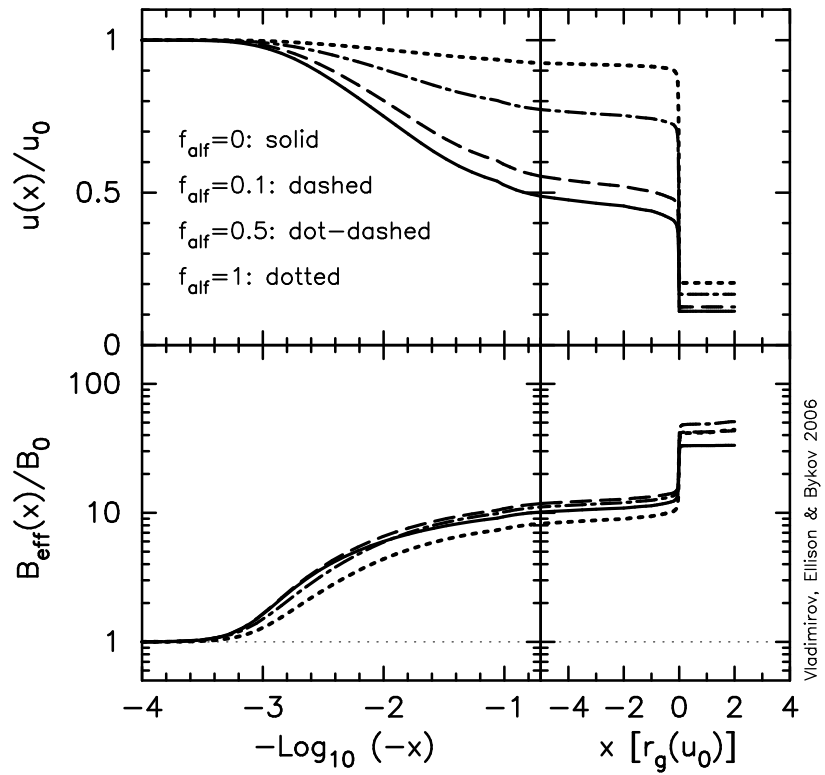


Fig. 7.— Shocks with varying f_{alf} as indicated. In all cases, $u_0 = 5000 \text{ km s}^{-1}$, $B_0 = 30 \mu\text{G}$, and $d_{\text{FEB}} = -1000 r_g(u_0)$.

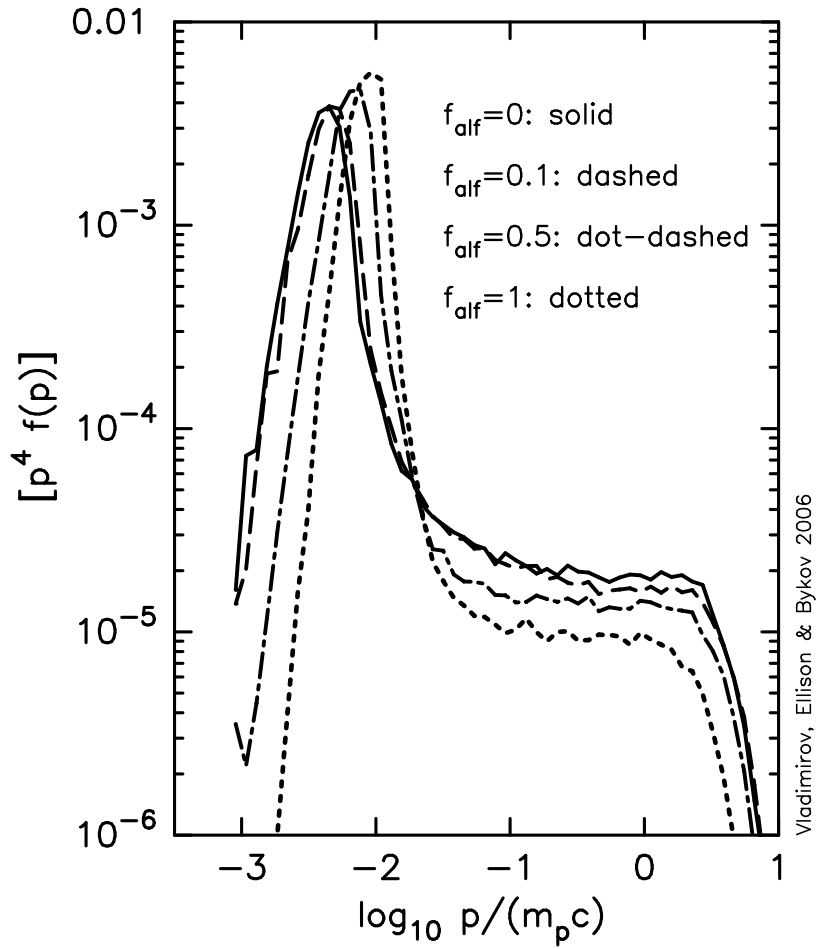


Fig. 8.— Distribution functions for the shocks shown in Figure 7 calculated downstream from the shock in the shock reference frame.

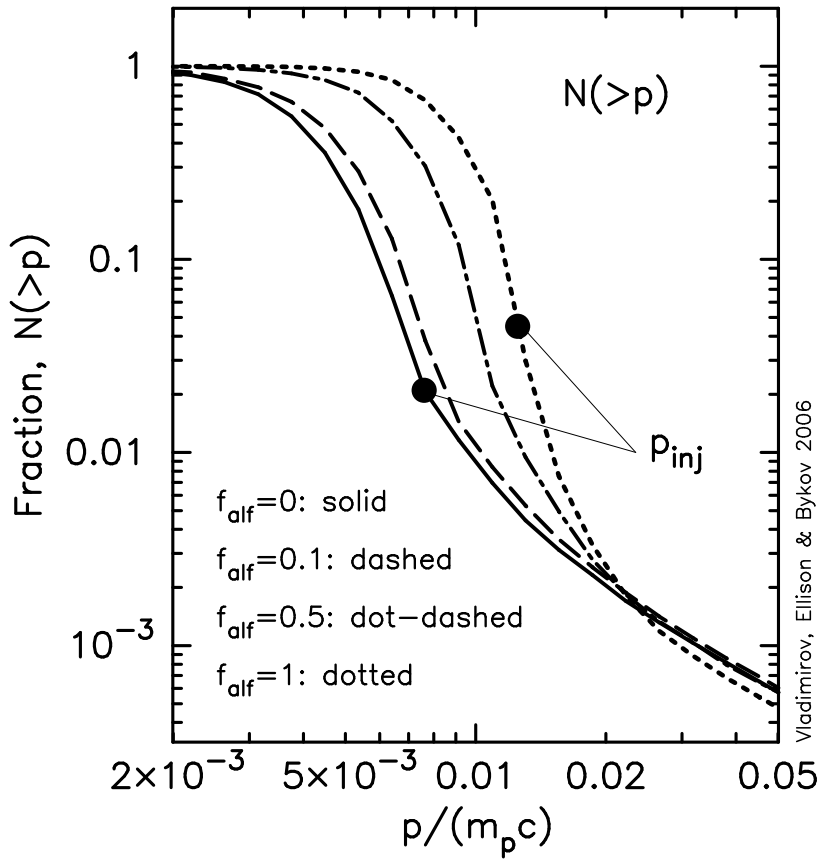


Fig. 9.— Injection efficiency in terms of the number of particles with momenta $> p$ for the four shocks shown in Figure 7. The solid dots give the approximate position for the transition between thermal and superthermal particles for the two extreme cases of $f_{\text{alf}} = 0$ and 1.